The influence of geometric defects and microstructure in the simulation of the mechanical behaviour of laser powder-bed fusion components: Application to endoprosthesis

The influence of geometric defects and microstructure in the simulation of the mechanical behavior of Laser Powder-Bed Fusion components: application to endoprosthesis.

Erica Liverani[a,*], Filippo Zanini[b], Lavinia Tonelli[a], Simone Carmignato[b], Alessandro Fortunato[a]

a Department of Industrial Engineering, University of Bologna, Bologna, Italy

b Department of Management and Engineering, University of Padua, Vicenza, Italy

* Corresponding author. E-mail address: erica.liverani2@unibo.it

Abstract

This work aims at enabling the fabrication of a new generation of prosthetic components with enhanced mechanical behaviour and an extended lifetime. Cobalt-chromium lattice structures manufactured using laser powder bed fusion are analysed to quantify the influence of microstructural anisotropy and geometrical deviations on stiffness prediction. Results of the experimental campaign are used to improve finite-element modelling of the mechanical behaviour of functionally graded lattice structures. The proposed method, which can be extended to any lattice structure fabricated by laser powder bed fusion, is then used to redesign an ankle prosthetic component.

Keywords

Additive Manufacturing, Functionally Graded Structures, Metrology, Microstructure, DIC, Modelling

1. Introduction

Laser powder bed fusion (LPBF) is an additive manufacturing (AM) process that enables the production of products characterized by high geometrical complexity [1]. Custom design is nowadays well-supported by a new generation of mathematical models for geometry development, as topology optimisation tools or generative design exploration processes [2]. Together with the possibility of optimising bulk components with the aforementioned software modules, AM processes, and in particular LPBF, enable the manufacturing of customizable lattice structures [3]. Lattice structures can be used in several applications [4-6], due to their potentialities: lightweight, customisation of mechanical properties and design of components with high surface/volume ratio. Among the others, lattices application includes the production of

personalized prosthetic components. In this sector, design and manufacturing innovations, made possible by LPBF, include the ability to obtain lighter components with adjustable stiffness that preserve bone stiffness values, while enhancing specific functional properties such as osseointegration [7]. Solid parts can be replaced with personalised light-weight structures with functionally graded stiffness [8].

The huge potential of these porous architected cellular materials is currently limited by concerns over their structural integrity, which mainly depends on accurate manufacturing and must consider several processes and material-related issues. LPBF products typically display anisotropic mechanical behaviour, which depends to a large extent on their unique microstructure characterised prevalently by epitaxial grains oriented in the build direction, inducing crystallographic texture [9]. In addition, such products often show significant discrepancies between as-designed and as-built geometry and dimensions [10]. These deviations are mostly due to the high temperature and fast heating and cooling cycles involved in LPBF, as well as the generation of a complex surface topography with high roughness [11, 12]. The characteristics of the feedstock material (i.e. metal powder) also have a significant influence on the final part properties [13]. Moreover, correct optimisation of LPBF process parameters for a specific material is often challenging [14]. As a consequence, internal defects such as lack-of-fusion pores or keyhole formation may arise, decreasing part density with a possible negative impact on mechanical properties [15]. This is a critical aspect, in particular for structures exposed to time-varying loads [16] as orthopaedic implants, which must meet the requirements of physiological load that is typically periodic and not constant over time [17]. All of these aspects undermine the reliability of finite element (FE) modelling based on nominal geometry for predicting lattice behaviour in the design phase [18].

The context of the present paper is the manufacturing of custom endoprostheses via LPBF. Nowadays, about 34% of orthopaedic implant replacements are due to failed osseointegration [19]. Several factors influence this type of failure, including the shape of the prosthesis, mismatch between the mechanical properties of the implant and bone, and stiffness at the implant-bone contact surface. The use of lattice structures is recognised as a valid approach to improve osseointegration and reduce stress-shielding phenomenon [20]. The effect of lattice unit design and geometrical density on the mechanical properties and interaction with biological tissues *in vitro* and *in vivo* has been properly investigated for Titanium alloys lattice structures [21,22], as well as the influence of geometrical inaccuracy and metallurgical defects [23]. Conversely, the

current knowledge on mechanical and biological performance of functionally graded Cobalt-chromium (CoCr) lattice [24,25] is limited.

For the reasons mentioned above, the lattice structures investigated in this paper are characterised by a variable hole size in the range of 0.5-1 mm, chosen to ensure cell viability, proliferation and colonization [26], and controlled lattice stiffness. Cobalt-chromium alloy is used for its biocompatibility and widespread use in endoprostheses and biomedical device production [27].

The main aim of this work is to investigate the effect of build strategy and lattice unit hole size on the mechanical properties and stiffness of CoCr LPBF lattice structures. In order to overcome adhesion issues of strain gauges on lattices and the positioning issues of mechanical extensometers, Digital Image Correlation (DIC) technique has been used for a contactless evaluation of deformations and for the stiffness measurement of the investigated structures.

An experimental campaign was conducted to determine the effects of unit geometry, geometrical inaccuracy and microstructure on stiffness behaviour of the lattices. The obtained results were used for improvement of FE models on lattice structures mechanical properties prediction. The presented methodology enables the design and fabrication of a new generation of custom endoprostheses that feature stiffness similar to human bones, reducing rejection due to stress shielding.

2. Materials and methods

2.1. Lattice structure production, testing and modelling

The single cell employed in the present study consisted of a cubic element with 1.5 mm edge perforated by three cylindrical through holes located at the centres of the cube faces (Fig. 1a). Three versions of the single cell were designed with different cylindrical hole diameters: 0.5 mm, 0.75 mm and 1 mm. The periodic samples, denoted S0.5, S0.75 and S1, respectively, were designed by repeating the same unit cell to obtain structures comprising 10 overlapping layers made up of 8×8 cells each (Fig. 1b).

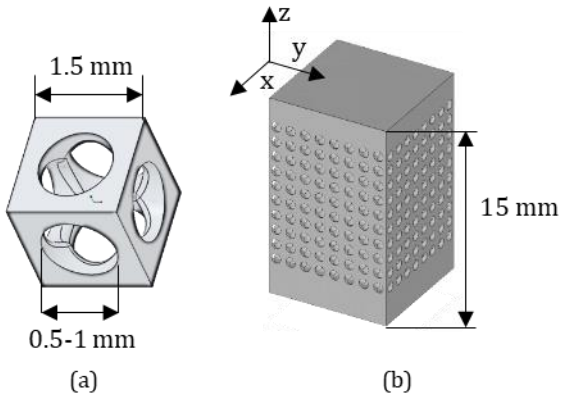

Figure 1. Geometry of single cell (a) and its repetition in test samples (b).

Ten samples of each type were manufactured by LPBF in CoCr alloy (Co28Cr6Mo), with five built in the z-direction and five in the x-direction. Spherical powder was supplied by Carpenter Technology (Philadelphia, US) in the standard dimension range of 15-45 µm. The powder had the following chemical composition: 27-30% Cr, 5-7% Mo, less than 1% Mg and Si, 0.75% Fe, less than 0.5% Ni, less than 0.1% other elements and the balance Co.

The AM machine used for sample fabrication was a SISMA MYSINT100 (Sisma SpA, Italy) with cylindrical building volume of 100 mm in diameter and 100 mm in height, equipped with fiber laser with spot size of 55 µm and maximum power of 175 W. Process parameters used for the investigation (summarised in Table 1) were chosen in accordance with [28] as the best trade-off between high part density and spatial resolution, with the latter required to be < 200 µm for the specific application at hand. All samples were built in a nitrogen environment with a residual oxygen content < 0.1 %.

Table 1. LPBF process parameters used for CoCr lattice structures production.

Laser power	Scan speed	Layer thickness	Hatch space	Scanning strategy
130 W	1200 mm/s	20 µm	70 µm	3×3 mm^2 chessboard

At the end of LPBF manufacturing and after parts detachment from the build platform and supports removal, the prismatic samples where grinded both on the supported surface and in the last printed layer, parallel to the building platform, in order to avoid any effects due to the flatness errors of the surfaces.

Compressive tests were performed with a servo hydraulic press (Italsigma, Forlì, Italy) equipped with a 100 kN load cell. Tests were performed in line with ISO 13314:2011 [29] for porous

materials at a strain rate of $5 \cdot 10^{-4}$ s^{-1}. Lattice samples used for mechanical tests were firstly prepared for DIC analysis with an artificial pattern deposited by spraying black paint dots on a white background. An acquisition program implemented in LabVIEW (National Instruments Corp., Texas) was used to store camera frames (6.4 MPx Basler acA3088-57µm) captured at constant load steps (5 kN for S0.5, 3 kN, for S0.75 and 1 kN for S1), which were subsequently processed using a commercial DIC software (GOM Correlate, GOM GmbH, Germany) to evaluate local displacements and strains. Images data processing then allowed calculation of the stiffness of each structure (k_{TOT}) and layer (k_{Layer}), as well as indirect calculation of the single unit stiffness (k_U) as the ratio between layer stiffness and the number of units per layer. A more exhaustive explanation of the procedure was described in a previous paper [30].

Comparison of experimental data with numerical results was carried out with an FE model developed in ANSYS (2020 R1). In order to reduce the computational load, only a quarter of the examined units were modelled, with plane symmetries and constraints as shown in Fig. 2a. The simulated element was discretised using a mesh dimension of 0.03 mm (Fig. 2b), determined with a mesh size sensitivity analysis.

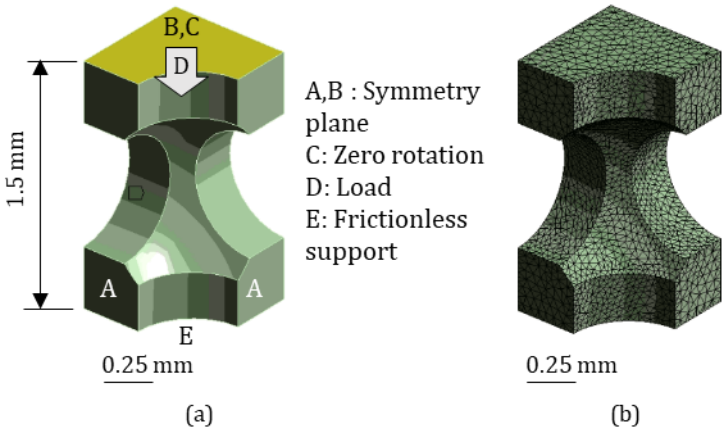

Figure 2. Simulated cell with load, constrains and symmetry boundary conditions (a) and mesh view model (b).

The Young's Modulus (E) and Poisson's coefficient (v) of Co28Cr6Mo used for FE simulations were measured with an ultrasonic through-transmission technique on full density LPBF samples produced with the same parameters as those employed for the lattice structures. An ultrasonic pulse-receiver (Karl Deutsch, Echograph 1095) was used to excite two ultrasonic transducers (2 MHz) and detect both longitudinal and shear waves, receiving signals reflected from the bottom surface of the metal specimen. E and v were then calculated as follows:

$$v = [1 - 2(V_T/V_L)^2] / [2 - 2(V_T/V_L)^2] \quad (1)$$

$$E = V_L^2 \rho(1 + v)(1 - 2v)/(1 - v) \quad (2)$$

where V_T and V_L are, respectively, the shear and longitudinal velocity [m/s] and ρ is the material density [kg/m^3]. The material density was determined for each sample using metrological X-ray computed tomography as described in Section 2.3.

2.2. Microstructural analysis

Microstructural characterization was carried out on metallographic sections extracted from lattice samples along the direction parallel to the applied compressive load. Samples were embedded in phenolic resin and subject to standard metallographic preparation, described in the ASTM E3-11 standard [31], concluding with mirror polishing with 1 µm diamond suspension. Prior to observation, metallographic sections were electrochemically etched with a solution of hydrochloric acid and ferric chloride in distilled water, as suggested in [32]. The microstructure was then observed both in bright field and under polarized light with an optical microscope (Axio Imager, Carl Zeiss Microscopy, Germany) to reveal the typical microstructural features, such as: melt pool borders, defects, epitaxial grains.

2.3. X-ray computed tomography analysis

Metrological X-ray computed tomography (CT) is an advanced three-dimensional (3D) measuring technique that is increasingly used for quality assessment of AM parts [33]. The main advantage of CT over conventional tactile and optical measuring techniques is its capability of performing non-destructive measurement of the external and internal geometry, micro-features (including defects) and surfaces [34]. In this work, measurements were performed on S0.5, S0.75 and S1 samples with 3×3×3 units with a metrological CT system (MCT225, Nikon Metrology, UK) characterized by a micro-focus X-ray source, 16bit detector with 2000×2000 pixels and temperature-controlled cabinet held at 20±0.5 °C. A total of 1800 bi-dimensional grey-scale projected images were acquired for each analysed sample, with a single frame per projection. The X-ray tube voltage was set at 215 kV, the current at 30 µA and the exposure time at 2000 ms, achieving a voxel size of 3.7 µm. A filtered back-projection algorithm was employed for 3D reconstruction of the volumetric models (see Fig. 5a,b,c). Visualization and analysis software VGStudio MAX 3.2 (Volume Graphics GmbH, Germany) was used for CT data processing. After

carrying out a surface determination procedure performed with an advanced local-adaptive algorithm, the internal porosity was evaluated in terms of volume, spatial distribution and shape. In addition, the actual geometry and dimensions of holes were measured and used to improve the FE simulations described in Section 2.1.

3. Results

3.1. Strain and stiffness measurements

Load-displacement curves obtained during compressive tests were firstly evaluated in order to determine the transition between elastic and plastic deformation. This threshold value was not defined following the definition of yield strength, but considering the real deviation of the load-displacement curve from the linearity of the elastic phase. Fig. 3 shows three exemplary curves, interrupted at a displacement of 1.5 mm for a better visualisation of the transition load. The following mean values were obtained for S0.5, S0.75 and S1, respectively: 35 kN, 24.5 kN and 10 kN.

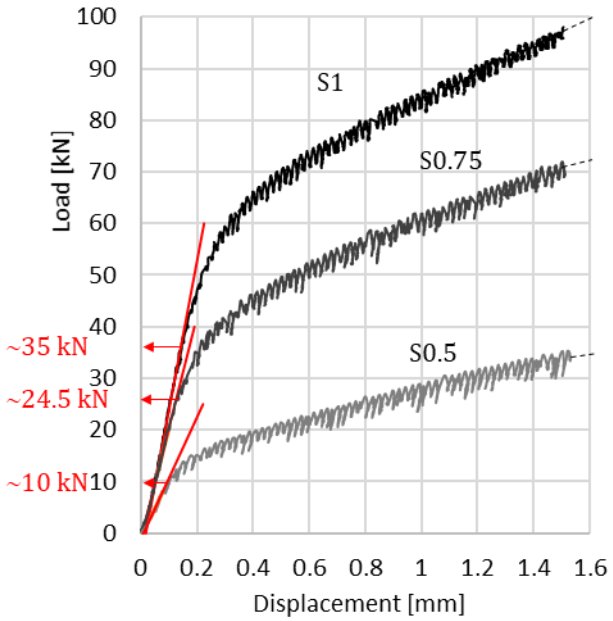

Figure 3. Example of load-displacement curves obtained for S0.5, S0.75 and S1and identification of the transition load between elastic and plastic behaviour.

Local displacement maps obtained from DIC analysis of each frame within the elastic deformation phase were then used to measure both the total and single layer displacement of each structure. In Fig.4 a displacement map comparison between S1 samples manufactured with opposite build direction (BD) is shown together with a schematic representation of the mentioned displacements. Both frames where captured at the same load during the elastic deformation

phase. From a preliminary and qualitative analysis of the two maps, it is possible to highlight a higher displacement of the S1 samples built in the z-direction (zBD) with respect to S1 samples built in the x-direction (xBD), which corresponds to lower stiffness values of the structure, as confirmed below.

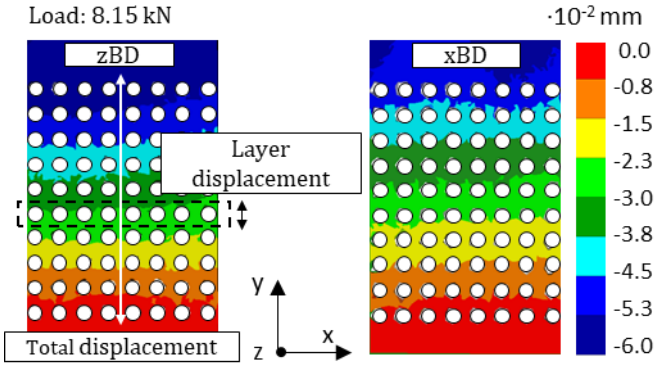

Figure 4. Total and single layer displacement measurement in S1 samples produced in opposite building directions: (left) zBD and (right) xBD.

Total and single unit stiffness values were then calculated in line with the procedure described in Section 2.1. Mean values obtained for all samples and frames are presented in Table 2, with the standard deviation in brackets.

Table 2. Experimental compressive stiffnesses. All values are in kN/mm.

	S1, zBD	S1, xBD	S0.75, zBD	S0.75, xBD	S0.5, zBD	S0.5, xBD
k_{TOT} (Std.Dev)	233 (69)	251 (8)	495 (84)	570 (103)	842 (112)	799 (26)
k_{Layer} (Std.Dev)	2013 (589)	2933 (379)	4749 (433)	6361 (1269)	6940 (1134)	8793 (204)
k_U (Std.Dev)	31.4 (9)	45.8 (6)	74.2 (7)	99.4 (20)	108.4 (18)	137.4 (3)

3.2. Microstructural anisotropy

The microstructures of representative samples built in the z and x-directions are shown in Fig. 5. Microstructures are compared on the basis of the compressive load direction, so as to discuss the effect of the microstructural features typical of LPBF on the mechanical behaviour. Low magnification microstructural analyses taken under polarized light (Fig. 5a,b) allow an overall observation of the microstructure, consisting of subsequent layers of melted and rapidly solidified metallic material. Layers are parallel to the build platform; therefore, when comparing the microstructure on the basis of the compressive load, they are differently oriented in the samples built in the z- (zBD, Fig. 5a) and x-direction (xBD, Fig. 5b). Each layer consists of successive almost

semi-circular melt pools, formed as a consequence of the localised melting of the powder bed induced by the laser beam. Melt pools are shown in higher detail in Fig. 5c,d, in which representative melt pool borders and epitaxial grain are underlined by yellow and white dashed lines, respectively. During the solidification of each melt pool, which develops very rapidly, grains grow following an epitaxial growth, thus they replicate the crystallographic orientation of the previous layer [35]. As a consequence of the epitaxial growth, long epitaxial grains crossing over layers and oriented in the build direction are formed, resulting in a highly oriented microstructure. Therefore, epitaxial grains, as highlighted in Fig. 5, are differently oriented among x- and z- built samples with reference to the applied load, as a consequence of the different build direction Such oriented epitaxial grains might induce a crystallographic texture that can affect elastic properties, such as stiffness, as already evidenced by previous work carried out on an additively manufactured austenitic stainless steels [36,37].

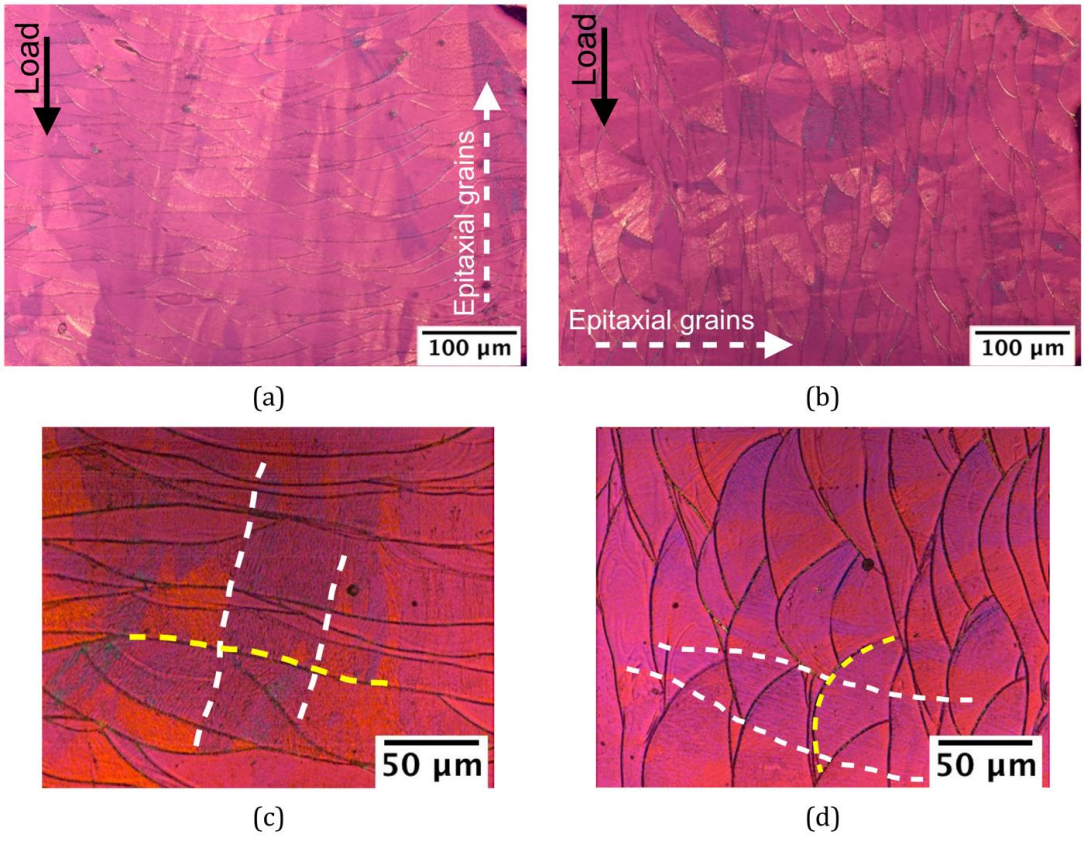

Figure 5. Optical micrographs taken under polarized light showing the representative microstructure of lattice structures of samples: (a), (c) low and high magnification of zBD and (b), (d) low and high magnification of xBD. White dashed lines outline epitaxial grains crossing over layers while yellow dashed lines outline melt pool borders.

As evidenced in previous study, the Co28Cr6Mo LPBF alloy consist of both Co-fcc and Co-hcp phases [38, 39] and literature shows that both fcc and hcp Co lattice structures are inherently

elastically anisotropic, thus they exhibit some crystallographic orientations stiffer than others [40,41]. The microstructural analyses so far discussed evidenced a different preferred crystallographic orientation in xBD and zBD samples, that can be responsible for the divergent stiffness. In addition, it should be also mentioned that typical microstructural defects induced by the process, such as lack-of-fusion (LOF) voids shown in Fig. 6, were detected in the samples. LOF usually form in correspondence of melt pool boundaries due to uncomplete melting and appear as irregularly shaped and elongated porosity, with presence of internal non-totally melted powder particles [42]. As a consequence of the different build directions, LOF are differently oriented between xBD and zBD samples. In detail, in zBD samples LOF were perpendicularly oriented to the applied load, on the contrary in xBD ones LOF lie along a direction almost parallel to the applied load. Therefore, it can be inferred that the different orientation of defects affected the actual cross-sectional area. In summary, as the microstructural features typical of the additive process (layers, epitaxial grains, LOF) strictly depend on the build orientation, the anisotropy found in the microstructure is due to the different orientation of the discussed features between samples build along the x- and z-direction.

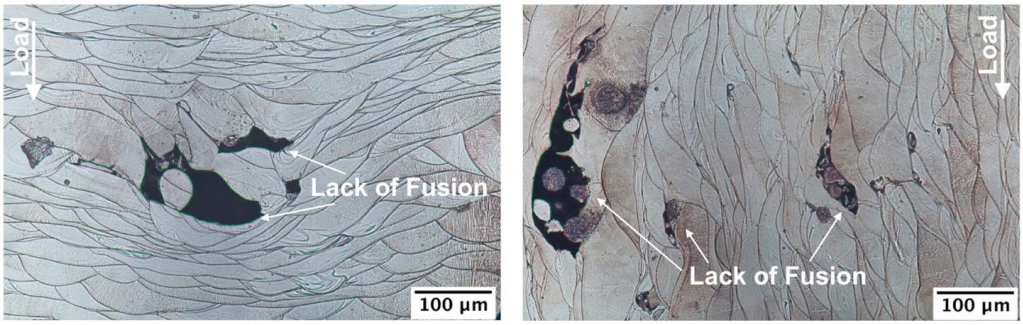

Figure 6. Microstructural discontinuities (i.e. lacks of fusion) differently oriented in: (a) zBD (b) xBD samples.

3.3. Internal porosity analysis

The porosity analysis performed with CT is shown in Fig. 7 d,e,f, where it can be seen that the porosity volume increases with decreasing hole size: 0.20% for S1, 0.53% for S0.75 and 0.97% for S0.5. The majority of larger voids is distributed in regions between the horizontal holes, presenting irregular shapes (see Fig. 8), typical of LOF porosity already evidenced by the above discussed microstructural analyses.

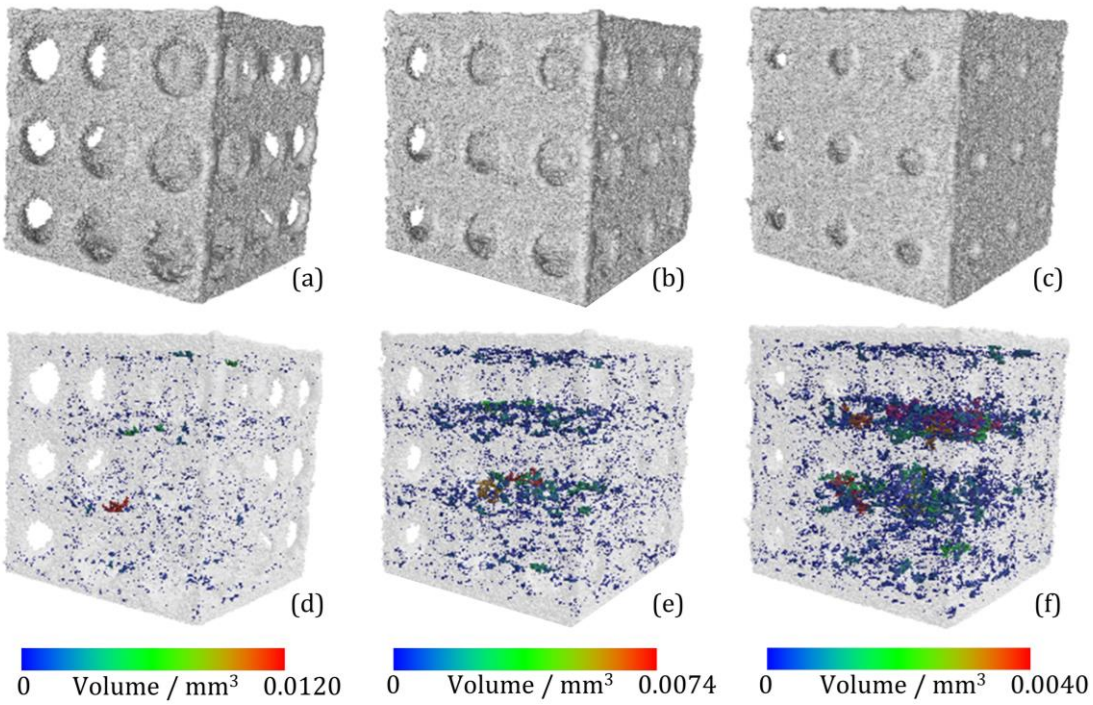

Figure 7. CT 3D reconstructions (top images) and porosity maps (bottom images) of samples S0.5 (a, d), S0.75 (b, e) and S1 (c, f).

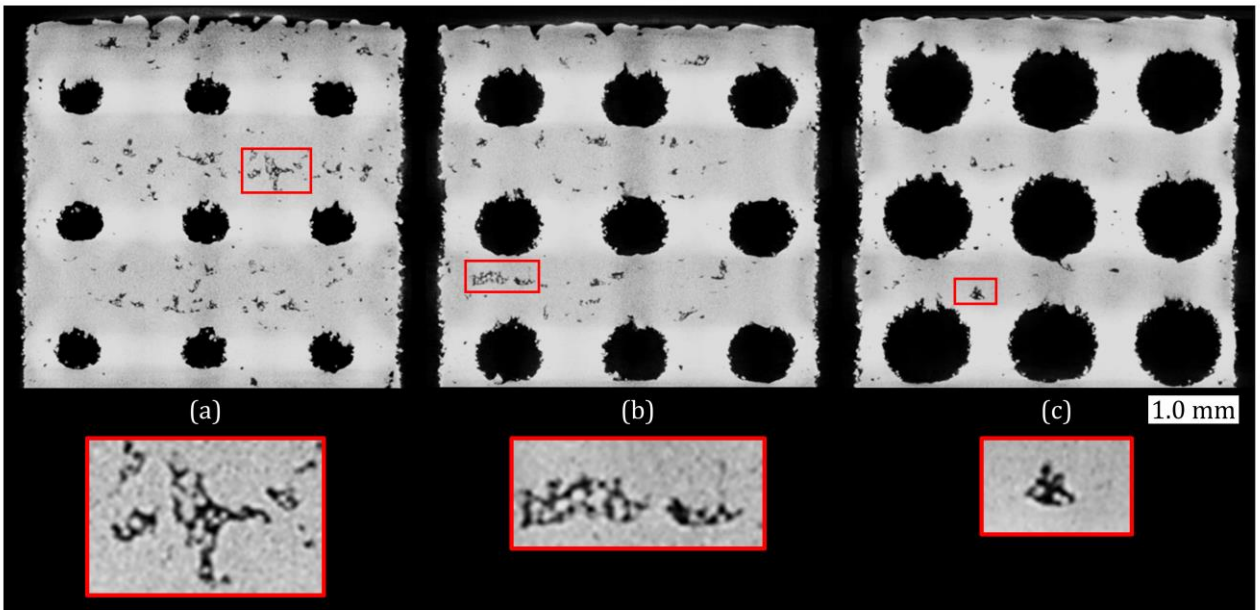

Figure 8. 2D cross-sections obtained from the CT data of samples S0.5 (a), S0.75 (b) and S1 (c). The major part of internal porosity is distributed in regions between the horizontal holes and presents irregular shapes with entrapped unmelted powder particles (typical of LOF voids), as visible in the zoomed examples shown in the red boxes at the bottom of each figure.

Following the calculation of the porosity related to each lattice structure, Young's modulus and Poisson's coefficient were calculated experimentally with Eq. 1 and 2 and reported in Table 3.

Table 3. Poisson's coefficient and Young's modulus measured by ultrasonic transmission technique.

V_L [m/s]	V_T [m/s]	ν	$E_{S0.5}$ [GPa]	$E_{S0.75}$ [GPa]	E_{S1} [GPa]
5779	3092	0.29	204.2	205.1	205.8

3.4. Geometrical and dimensional measurements

Cross-sections of holes were extracted from CT reconstructions, examples of which are presented in Fig. 9. Least-squares circles and ellipses were fitted to the borders of hole's sections, which were determined using a local-adaptive surface determination algorithm (see Fig. 9). It can be observed that for all samples, circles and ellipses are almost superimposed when the hole axis is parallel to the AM build direction (zBD), but are significantly different when the hole axis is perpendicular to the build direction (xBD) due to dross formation, typically occurring on down-facing LPBF surfaces [43]. This observation is further confirmed by results reported in Tab. 4.

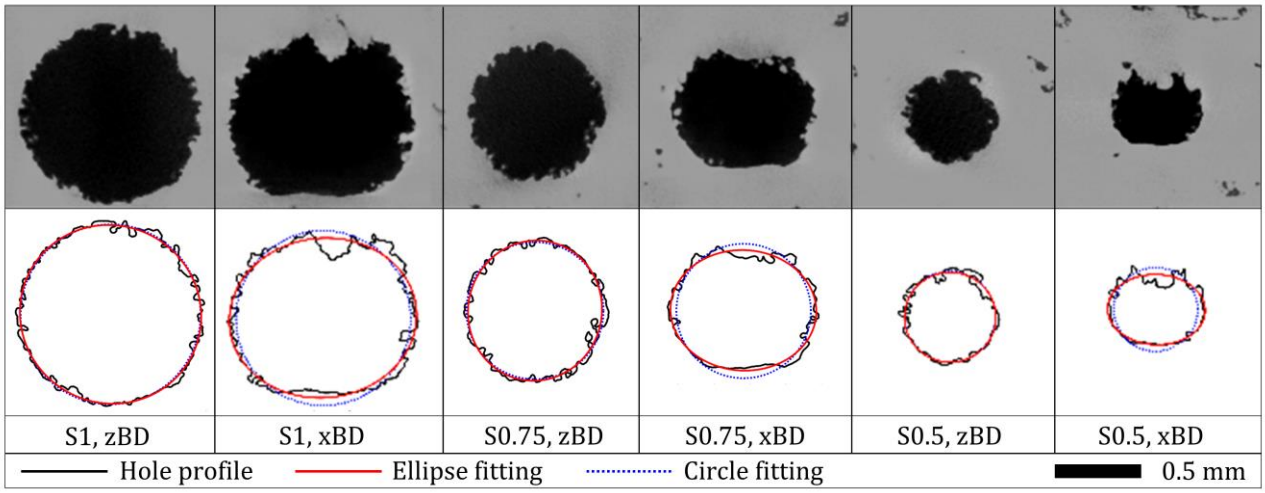

Figure 9. Examples of hole cross-sections extracted from CT reconstructions (top images) and determined hole profiles with circles and ellipses obtained by least-squares fitting (bottom images).

Table 4. Example of circle (C) diameters and ellipse (EL) maximum and minimum axis dimensions measured from hole cross-sections.

Dimensions in mm	S1 zBD	S1 xBD	S0.75 zBD	S0.75 xBD	S0.5 zBD	S0.5 xBD
C diameter	1.006	0.976	0.765	0.750	0.507	0.468
EL max axis	1.021	1.048	0.746	0.672	0.511	0.392
EL min axis	0.992	0.891	0.785	0.814	0.502	0.545

3.5. Simulation results

FE simulations were performed with both theoretically circular holes and the actual shape of holes derived from CT measurements (as illustrated in Section 3.4). An example of FE results in terms of displacement is shown in Fig. 10. S0.75 with circular hole (Fig. 10a, representing the originally designed shape) and elliptical hole (Fig. 10b, approximating the real shape) lattice units are compared at the same load and the maximum values of displacement were calculated and compared. Similar analysis was carried out for all three geometries and the obtained outcomes are presented in Fig. 11 together with the experimental results.

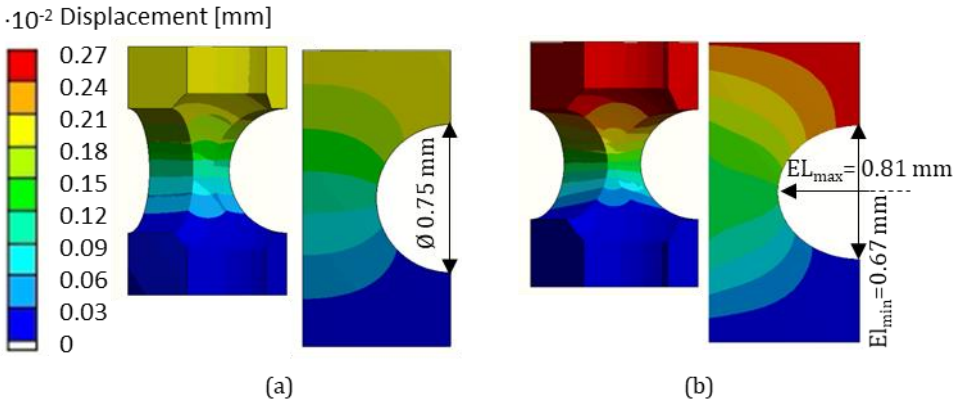

Figure 10. FE displacement prediction of S0.75 lattices with circular (a) and elliptical (b) hole.

A preliminary consideration that is worth making concerns the comparison between elementary units: by increasing the size of holes the stiffness of structures decreases down to 31.4-45.8 kN/mm, approaching the stiffness of cortical bone (10 kN/mm). Considering results relating to cell viability, proliferation and colonization reported in [28] and the target of stress shielding reduction in orthopaedic [44], the values obtained with the proposed units are relevant to the proposed application. As concern the main aim of this work, more specific results can be obtained from the comparison between designed and real structures and considering the effect of build direction,

which affect the microstructure of the lattices, on unit cell stiffness. To this end, relevant considerations can be summarized as follows:

1. zBD structures exhibit a lower stiffness than xBD structures, with the deviation between values in the range 21-31%.
2. The simulated stiffness obtained with ideal circular holes is higher than the experimental stiffness, on average by 20% when compared to the stiffness of samples with xBD and 41% when compared to those with zBD.
3. When the simulations are repeated considering the actual shape of holes as derived from CT measurements, the predicted stiffnesses becomes similar to experimental data for xBD (max deviation reduced to 10%)

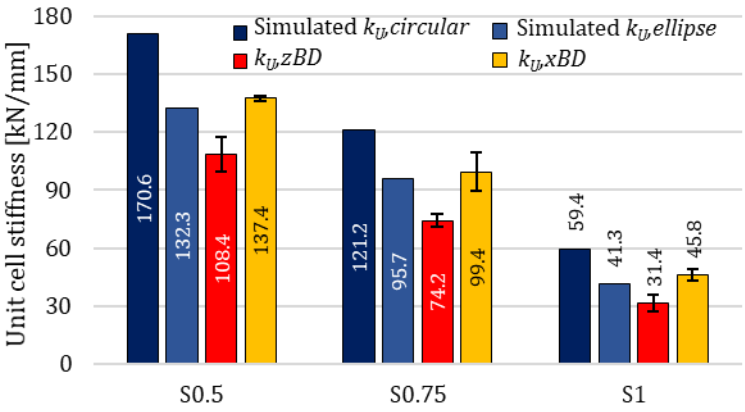

Figure 11. Theoretical stiffness calculated by FE simulations and comparison with experimental data.

4. Discussion

By considering the results presented above, three main differences were observed between samples: (i) microstructural anisotropy depending on the build strategy, (ii) differences in porosity and (iii) geometrical and dimensional deviations.

Microstructural analyses, in fact, showed long epitaxial grains crossing over layers, directed along the build direction. Consequently, epitaxial grains were oriented differently in zBD and xBD lattice structures with respect to the applied compressive load, inducing anisotropy in the mechanical response. This microstructural feature can explain the reduction in stiffness (on average 25%) of lattice structures subject to loads perpendicular to the BD.

Metrological CT analyses revealed a concentration of lack-of-fusion porosity, as well as an ellipse-like shape of holes section when the hole axis is perpendicular to the build direction, differing from the nominal circular shape. A significant variation in porosity between different lattice units

was observed despite process parameters remaining unchanged. In particular, the number and average dimensions of pores increased with decreasing hole dimensions. This can be primarily due to the lower heat exchange in the case of lighter structures, maintaining higher temperatures and lower thermal gradients during production and hence promoting correct melting of the powder. However, it is important to underline two aspects: (i) the percentage content of porosity is below 1% of the total analysed matter volume for all the samples and (ii) porosity is not the main cause of fracture for the axial compressive loads applied in this work. The latter aspect was proven by the fact that the actual ellipse-like shape of hole's sections was found to be the principal cause of reduced stiffness with respect to the simulation data based on nominal circular hole's sections. Correction of the hole geometry in the FE model led to a decrease in stiffness of up to 30%, making the theoretical data better comparable to experimental values obtained for xBD lattice structures.

These considerations allowed the effect of geometrical deviations and microstructural anisotropy on theoretical / experimental mismatch to be quantified. Geometrical deviations of the hole section shape were found to be responsible for deviations between the stiffness calculated with FE simulations and measured values for xBD samples, with a mean contribution to the total error of 55%. Microstructural anisotropy could be identified as the deviation between the two build directions, with an influence on the total error estimated to be 45%. Considering all of the aforementioned results, it is possible to account for these differences in any FE software by introducing a correction to ensure valid prediction with the use of conventional mechanical models. This correction is introduced with a constant coefficient for each BD: 0.55 for z and 0.80 for x. Intermediate BD and loading directions would require corrections within this range, as the cited values represent the minimum and maximum deviation between real and simulated data. Introducing this correction into FE software may allow improvement in the design of lattice structures to achieve desired properties with high accuracy.

These concepts were successfully applied to the design of an endoprosthesis with functionally graded lattice structures, shown in Fig. 12.

The stiffness varies from a maximum value, corresponding to full density, to lower values obtained with S1 units, close to that of human bone. The proximity of the implant and bone stiffness in the contact area reduces the risk of stress shielding by decreasing the probability of failure. The proposed method can be generalized for the design of any lattice structure.

However, the proposed model needs further improvement with particular attention in computational cost reduction in case of complex lattice structures. Furthermore, the mechanical behavior of lattice structures and the influence on model discrepancy should consider the real physiological load condition. Future efforts should upgrade the proposed model by considering both of these aspects and integrating it with the design optimization of customized endoprosthesis.

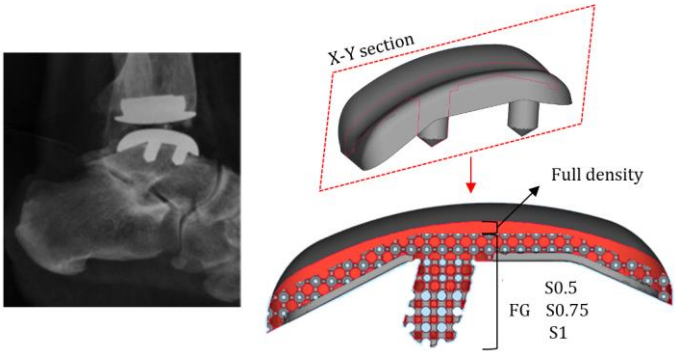

Figure 12. Example of post-implant X-ray image [45] of a commercial full density ankle prosthesis (left), and functionally graded (FG) structure with optimized design (right).

5. Conclusion

This paper investigated the influence of LPBF on the mechanical behaviour of lattice structures in order to optimize the design and fabrication of cobalt-chromium prosthetic components. The mean difference in stiffness between theoretical and experimental values was evaluated as 40 %. This variation was further investigated through different analyses and the following results were obtained: (i) 45% of this variation is due to microstructural anisotropy and (ii) 55% is due geometrical deviation. In particular, the hole shape was determined to cause a stiffness reduction of 30% for single units. Based on the obtained results, an FE model for the design and fabrication of lattice structures could be improved. Reliable prediction of the stiffness of elementary units allows assessment of the properties of entire structures with complex macro-geometry that can be designed by locally varying the stiffness. These results were applied to a preliminary prototype of custom joint prostheses with good outlook in the reduction of implant failure due to stress shielding, as lattice structures with a minimum stiffness of 31.4 kN/mm were obtained, very close to cortical bone stiffness of 10 kN/mm. The proposed method can be further extended to the design of generic lattice structures.

References

[1] Gibson I, Rosen D, Stucker B, Khorasani M. Additive manufacturing technologies. New York: Springer 2021.

[2] Ranjan R, Ayas C, Langelaar M, van Keulen F. Topology Optimisation Techniques. In book: Precision Metal Additive Manufacturing. CRC Press 2020.

[3] Hanks B, Berthel J, Frecker M, Simpson T W. Mechanical properties of additively manufactured metal lattice structures: Data review and design interface. Additive Manufacturing 2020; 35: 101301. https://doi.org/10.1016/j.addma.2020.101301

[4] Ju Yeo S, Jun Oh M, Yoo P J. Structurally Controlled Cellular Architectures for High-Performance Ultra-Lightweight Materials. Advanced Materials 2018; 31(34): 1803670 https://doi.org/10.1002/adma.201803670

[5] Ibrahim Y, Li Z, Davies C M, Maharaj C, Dear J P, Hooper P A. Acoustic resonance testing of additive manufactured lattice structures. Additive Manufacturing 2018. 24:566-576. https://doi.org/10.1016/j.addma.2018.10.034

[6] Kaur I, Singh P. Critical evaluation of additively manufactured metal lattices for viability in advanced heat exchangers. International Journal of Heat and Mass Transfer 2021. 168: 120858. https://doi.org/10.1016/j.ijheatmasstransfer.2020.120858

[7] Bing R, Yi W, Chao L, Hongwei W, Mingzhi Y, Xiao Z, Yong H. Improved osseointegration of 3D printed Ti-6Al-4V implant with a hierarchical micro/nano surface topography: An in vitro and in vivo study. Materials Science and Engineering: C 2021. 118: 111505. https://doi.org/10.1016/j.msec.2020.111505

[8] Chashmi M J, Fathi A, Shirzad M, Jafari-Talookolaei R A, Bodaghi M, Rabiee S M. Design and analysis of porous functionally graded femoral prostheses with improved stress shielding. Designs 2020. 4: 1-15. https://doi.org/10.3390/designs4020012

[9] DebRoy T, Wei H L, Zuback J S, Mukherjee T, Elmer J W, Milewski J O, Beese A M, Wilson-Heid A, De A, Zhang W. Additive manufacturing of metallic components – Process, structure and properties. Prog. Mater. Sci. 2018, 92: 112-224. https://doi.org/10.1016/j.pmatsci.2017.10.001

[10] Maconachie T, Leary M, Lozanovski B, Zhang X, Qian M, Faruque O, Brandt M. SLM lattice structures: Properties, performance, applications and challenges. Materials & Design 2019. 183: 108137.

[11] Hooper, P. A. (2018). Melt pool temperature and cooling rates in laser powder bed fusion. Additive Manufacturing, 22, 548-559. https://doi.org/10.1016/j.matdes.2019.108137

[12] Zanini F, Pagani L, Savio E, Carmignato S. Characterisation of additively manufactured metal surfaces by means of X-ray computed tomography and generalised surface texture parameters. CIRP annals 2019. 68(1): 515-518. https://doi.org/10.1016/j.cirp.2019.04.074

[13] Cordova L, Bor T, de Smit M, Carmignato S, Campos M, Tinga T. Effects of powder reuse on the microstructure and mechanical behaviour of Al–Mg–Sc–Zr alloy processed by laser powder bed fusion (LPBF). Additive Manufacturing 2020. 36: 101625. https://doi.org/10.1016/j.addma.2020.101625
[14] Oliveira J P, LaLonde A D, Ma J. Processing parameters in laser powder bed fusion metal additive manufacturing. Materials Design 2020. 193: 108762. https://doi.org/10.1016/j.matdes.2020.108762
[15] Ronneberg T, Davies C M, Hooper P A. Revealing relationships between porosity, microstructure and mechanical properties of laser powder bed fusion 316L stainless steel through heat treatment. Materials & Design 2020. 189: 108481. https://doi.org/10.1016/j.matdes.2020.108481
[16] Benedetti M, Dallago M, du Plessis A, Ritchie R O, Razavi S M J, Berto F. Architected cellular materials: A review on their mechanical properties towards fatigue-tolerant design and fabrication. Materials Science and Engineering: R: Reports 2021. 144: 100606. https://doi.org/10.1016/j.mser.2021.100606
[17] Baleani M, Cristofolini L, Viceconti M. Endurance testing of hip prostheses: a comparison between the load fixed in ISO 7206 standard and the physiological loads. Clinical Biomechanics 1999. 14(5):339-45. https://doi.org/10.1016/S0268-0033(98)00085-0
[18] Schmidt M, Merklein M, Bourell D, Dimitrov D, Hausotte T, Wegener K, Overmeyer L, Vollertsen F, Levy G N. Laser based additive manufacturing in industry and academia. CIRP Annals 2017. 66/2: 561-583. https://doi.org/10.1016/j.cirp.2017.05.011
[19] Lum Z C, Shieh A K, Dorr L D. Why total knees fail-A modern perspective review. World J Orthop 2018 9(4): 60-64. https://doi.org/10.5312/wjo.v9.i4.60
[20] Goriainov V, Cook R, Latham J M, Dunlop D G, Oreffo R O. Bone and metal: An orthopaedic perspective on osseointegration of metals. Acta Biomater 2014. 10(10): 4043–4057. https://doi.org/10.1016/j.actbio.2014.06.004
[21] Shi J, Liang H, Jiang J, Tang W, Yang J. Design and performance evaluation of porous titanium alloy structures for bone implantation. Math. Probl. Eng. 2019. doi: 10.1155/2019/5268280
[22] Zaharin H A, Rani A M A, Azam F I, Ginta T L, Sallih N, Ahmad A, Yunus N A, Zulkifli T Z A. Effect of unit cell type and pore size on porosity and mechanical behavior of additively manufactured Ti6Al4V scaffolds. Materials 2018. 11(12): E2402. https://doi.org/10.3390/ma11122402
[23] Dallago M, Winiarski B, Zanini F, Carmignato S, Benedetti M. On the effect of geometrical imperfections and defects on the fatigue strength of cellular lattice structures additively manufactured via Selective Laser Melting. International Journal of Fatigue 2019. 124: 348-360. https://doi.org/10.1016/j.ijfatigue.2019.03.019
[24] Mahmoud D, Elbestawi M. Lattice Structures and Functionally Graded Materials Applications in Additive Manufacturing of Orthopedic Implants: A Review. J. Manu. Mater. Proces. 2017. 1(2): 13. https://doi.org/10.3390/jmmp1020013

[25] Pagani S, Liverani E, Giavaresi G, De Luca A, Belvedere C, Fortunato A, Leardini A, Fini M, Tomesani L, Caravaggi P. Mechanical and in vitro biological properties of uniform and graded Cobalt-chrome lattice structures in orthopedic implants. J Biomed Mater Res B Appl Biomater. 2021. https://doi.org/10.1002/jbm.b.34857.

[26] Van Bael S, Chai Y C, Truscello S, Moesen M, Kerckhofs G, Van Oosterwyck H, Kruth J P, Schrooten J. The effect of pore geometry on the in vitro biological behavior of human periosteum-derived cells seeded on selective laser-melted Ti6Al4V bone scaffolds. Acta Biomater 2012. 8(7): 2824-2834. https://doi.org/10.1016/j.actbio.2012.04.001

[27] Navarro M, Michiardi A, Castaño O, Planell J A. Biomaterials in orthopaedics 2008. 5(27) https://doi.org/10.1098/rsif.2008.0151

[28] Caravaggi P, Liverani E, Leardini A, Fortunato A, Belvedere C, Baruffaldi F, Fini M, Parrilli A, Mattioli-Belmonte M, Tomesani L, Pagani S. CoCr porous scaffolds manufactured via selective laser melting in orthopedics: Topographical, mechanical, and biological characterization. J Biomed Mater Res B Appl Biomater 2019. 107(7): 2343-2353. https://doi.org/10.1002/jbm.b.34328.

[29] ISO 13314:2011. Mechanical testing of metals - Ductility testing - Compression test for porous and cellular metals. 2011. https://www.iso.org/standard/53669.html.

[30] Liverani E, Fortunato A. Stiffness prediction and deformation analysis of Cobalt-Chromium lattice structures: From periodic to functionally graded structures produced by additive manufacturing. Journal of Manufacturing Processes 2021. 68: 104-114. https://doi.org/10.1016/j.jmapro.2021.05.033

[31] ASTM E3-11. Standard Guide for Preparation of Metallographic Specimens. 2017. https://www.astm.org/Standards/E3.htm

[32] Klarstrom D, Crook P, Wu J. Metallography and Microstructures of Cobalt and Cobalt Alloys, in: G.F. Vander Voort (Ed.), Metallogr. Microstruct. - ASM Handb. Vol.9, ASM International, 2004: pp. 762–774. doi:10.31399/asm.hb.v09.a0003771

[33] Baier M, Sinico M, Witvrouw A, Dewulf W, Carmignato S. A novel tomographic characterisation approach for sag and dross defects in metal additively manufactured channels. Additive Manufacturing 2011. 39: 101892. https://doi.org/10.1016/j.addma.2021.101892

[34] Hermanek P, Zanini F, Carmignato S. Traceable Porosity Measurements in Industrial Components Using X-Ray Computed Tomography. Journal of Manufacturing Science and Engineering 2019. 141(5): 051004. https://doi.org/10.1115/1.4043192

[35] Basak A, Das S. Epitaxy and Microstructure Evolution in Metal Additive Manufacturing. Annu. Rev. Mater. Res. 2016. 46: 125–149. doi:10.1146/annurev-matsci-070115-031728.].

[36] Laghi V, Tonelli L, Palermo M, Bruggi M, Sola R, Ceschini L, Trombetti T. Experimentally-validated orthotropic elastic model for Wire-and-Arc Additively Manufactured stainless steel. Addit. Manuf. 2021. 101999. doi:10.1016/j.addma.2021.101999

[37] Kyvelou P, Slack H, Mountanou D D, Wadee M A, Ben Britton T, Buchanan C, Gardner L. Mechanical and microstructural testing of wire and arc additively manufactured sheet material. Mater. Des. 2020. 192: 108675. doi:10.1016/J.MATDES.2020.108675

[38] Tonelli L, Fortunato A, Ceschini L. CoCr alloy processed by Selective Laser Melting (SLM): effect of Laser Energy Density on microstructure, surface morphology, and hardness. J. Manuf. Process. 2020. 52: 106–119. doi:10.1016/j.jmapro.2020.01.052

[39] Molinari A. The structural metastability of metallic alloys produced by Selective Laser Melting. La Metall. Ital. 2017. 1: 21–27.

[40] Desmond T. ELASTIC ANISOTROPY OF HCP METAL CRYSTALS AND POLYCRYSTALS. IJRRAS 2011. 6(4).

[41] Gump J, Xia H, Chirita M, Sooryakumar R, Tomaz M A, Harp G R. Elastic constants of face-centered-cubic cobalt. Journal of Applied Physics 1999. 86: 6005. https://doi.org/10.1063/1.371647

[42] DebRoy T, Wei H L, Zuback J S, Mukherjee T, Elmer J W, Milewski J O, Beese A M, Wilson-Heid A, De A, Zhang W. Additive manufacturing of metallic components – Process, structure and properties. Prog. Mater. Sci. 2018. 92: 112–224. doi:10.1016/j.pmatsci.2017.10.001.

[43] Klingaa C G, Zanini F, Mohanty S, Carmignato S, Hattel J H. Characterization of geometry and surface texture of AlSi10Mg laser powder bed fusion channels using x-ray computed tomography. Applied Sciences 2021. 11(9): 4304. https://doi.org/10.3390/app11094304

[44] Prochor P, Frossard L Sajewicz E. Effect of the material's stiffness on stress-shielding in osseointegrated implants for bone-anchored prostheses: a numerical analysis and initial benchmark data. Acta of bioengineering and biomechanics 2020. 22(2):69-81. 10.37190/ABB-01543-2020-02

[45] Lullini G, Caravaggi P, Leardini A, Ortolani M, Mazzotti A, Giannini S, Berti L. Retrospective comparison between a two- and three-component ankle arthroplasty: clinical and functional evaluation via gait analysis. Clinical Biomechanics 2020. 80-105180. 10.1016/j.clinbiomech.2020.105180